# Controlling protein nanocage assembly with hydrostatic pressure

*Kristian Le Vay[1,2], Ben M. Carter[3], Daniel W. Watkins[1], T-Y. Dora Tang[1], Valeska P. Ting[4], Helmut Cölfen[5], Robert P. Rambo[6], Andrew J. Smith[6], J. L. Ross Anderson*[1,7], Adam W. Perriman*[3]*

[1]School of Biochemistry, University of Bristol, University Walk, Bristol, BS8 1TD, UK.

[2]Bristol Centre for Functional Nanomaterials, HH Wills Physics Laboratory, University of Bristol, Tyndall Avenue, Bristol, BS8 1TL, UK.

[3]School of Cellular and Molecular Medicine, University of Bristol, University Walk, Bristol, BS8 1TD, UK.

[4]Bristol Composites Institute (ACCIS), University of Bristol, Queen's Building BS8 1TR, UK

[5]Department of Chemistry, University of Konstanz, Universitätsstraße 10, 78457 Konstanz, Germany

[6]Diamond Light Source Ltd., Diamond House, Harwell Science and Innovation Campus, Fermi Ave, Didcot OX11 0DE, UK

[7]BrisSynBio Synthetic Biology Research Centre, Life Sciences Building, University of Bristol, Tyndall Avenue, Bristol, BS8 1TQ, UK.

*Email: ross.anderson@bristol.ac.uk, chawp@bristol.ac.uk

**Controlling the assembly and disassembly of nanoscale protein cages for the capture and internalisation of protein or non-proteinaceous components is fundamentally important to a diverse range of bionanotechnological applications. Here, we study the reversible, pressure-induced dissociation of a natural protein nanocage, *E. coli* bacterioferritin (Bfr), using synchrotron radiation small angle X-ray scattering (SAXS) and circular dichroism (CD). We demonstrate that hydrostatic pressures of 450 MPa are sufficient to completely dissociate the Bfr icositetramer into protein dimers, and the reversibility and kinetics of the reassembly process can be controlled by selecting appropriate buffer conditions. We also demonstrate that the heme B prosthetic group present at the subunit dimer interface influences the stability and pressure lability of the cage, despite its location being discrete from the inter-dimer interface that is key to cage assembly. This indicates a major cage-stabilising role for heme within this family of ferritins.**

Nanoscale protein cages are attractive scaffolds for bionanotechnology and materials science, where they can be exploited as platforms for constructing robust and configurable therapeutic delivery vectors[1], vaccines[2], nanoreactors[3,4] and templates for the synthesis of diverse nanomaterials[5–8]. These multifunctional containers, both natural[9–13] and designed[14,15], offer unparalleled control over size, shape, microenvironment, surface functionalisation and stability when constructing novel bionanomaterials.

The ability to control the assembly of such nanocages is an invaluable tool in the synthesis of complex materials, and can be instrumental in facilitating the

48  encapsulation of non-native nanomaterials. While this can be achieved by exploiting

49  natural[16–18] or engineered[19–21] cage metastability, the use of such nanocages could

50  ultimately compromise the robustness of the final assembled material. For nanocages

51  with higher relative stability, harsher environmental conditions[22,23] are required that

52  can adversely affect the protein cage, its functional modifications or the intended

53  payload for encapsulation. Therefore, new methods are required to circumvent the

54  necessity for harsh chemical conditions or specific interfacial engineering to promote

55  cage instability, and to realise the full potential of these cages in bionanotechnology.

56

57  Here, we report on how hydrostatic pressure can be employed to control the

58  disassembly and reassembly of the protein nanocage bacterioferritin from *E. coli* (Bfr).

59  While hydrostatic pressure has been previously employed to dissociate the weakly

60  stable cage-like assembly HSP26[24],  the structure is not truly hollow[25]. There are

61  currently no reports of complete, reversible hydrostatic pressure-induced dissociation

62  in a highly robust nanocage such as ferritin[26,27]. While hydrostatic pressure has been

63  applied to human ferritin to facilitate the loading of doxorubicin and increase protein

64  recovery[27], the assembly/disassembly of the cage under pressure was not

65  investigated. Specifically, we use synchrotron radiation small angle X-ray scattering

66  (SAXS)[28] to show that the Bfr nanocage dissociates reversibly under pressure, and

67  that the reassembly can be controlled by altering solution conditions. Hydrostatic

68  pressures of 450 MPa were sufficient to induce reversible dissociation of the Bfr

69  icositetramer into subunit dimers, and the reversibility of the pressure-induced

70  dissociation was found to be highly dependent on ionic strength and temperature,

71  allowing for control of oligomerisation state through pressurisation and selection of

72  buffer conditions. Furthermore, we demonstrate that the pressure lability of the

73    nanocage can be modulated by removal of the native heme B prosthetic group. Our

74    study exploits the ability of SAXS to probe the quaternary, tertiary and secondary

75    structure of proteins, and will provide not only the means for studying the

76    supramolecular assembly of these highly valuable nanocages, but also inform future

77    methodologies for controlling protein nanocage assembly for efficient payload

78    encapsulation.

79

80    **Results & Discussion**

81    We initially probed the pressure-induced dissociation of the core-free, or apo-,

82    bacterioferritin icositetramer (ABfr) by gradually raising the applied hydrostatic

83    pressure in a diamond-windowed SAXS pressure cell to 450 MPa in 25 MPa

84    increments, equilibrating for 300 seconds prior to data collection at each pressure. An

85    undulating scattering pattern was observed at low pressures (Figure 1a), characteristic

86    of the hollow nanocage structure. With increasing pressure, fringes corresponding to

87    the hollow sphere form factor broaden and then disappear, indicating increasing

88    polydispersity and decreasing concentration of icositetramer due to dissociation into

89    lower order oligomeric species. The presence of isosbestic points in the reciprocal

90    space and Kratky data (Figure 1a and 1b), indicates that two species contribute to I($q$)

91    with proportional stoichiometry. At higher pressures (> 300 MPa), a slight drift in the $q$

92    value of the isosbestic points is observed, suggesting additional species likely

93    contribute to the dissociation process.

94

95    From the pair distance distribution factor ($P(r)$), we determined the radius of gyration,

96    $R_g$ (Figure 1c), which decreases non-linearly from 50 Å to 32 Å over the pressures

97    applied here (Figure 1d). This non-linear change in $R_g$ with pressure is due to the

98  power law dependence of $R_g$ upon number of residues in the scattering particle[29],

99  rather than suggesting a cooperative dissociation mechanism. The data therefore

100 indicate gradual icositetramer dissociation with multiple intermediates, and a final state

101 in which the majority of species are small subunit oligomers. The *P(r)* distribution of

102 ABfr is characteristic of a hollow sphere until 250 MPa. The maximum of this

103 distribution, $P(r)_{max}$ ($r$ = 84 Å), corresponds to the expected chord length for a hollow

104 sphere and decreases steadily with pressure, indicating gradual loss of the

105 icositetramer. At higher pressures, the magnitude at $r$ = 84 Å tends to zero and a new

106 $P(r)_{max}$ emerges at $r$ = 32 Å, corresponding to a subunit oligomer of ABfr previously

107 masked by the fully assembled cage. Importantly, the maximum observed diameter,

108 $D_{max}$, never exceeds the atmospheric pressure value, suggesting that aggregates of

109 intact ABfr particles do not form at higher pressures and that dissociation of the particle

110 into smaller oligomers predominates.

111

112 Using a linear combination of theoretical SAXS data from various oligomeric

113 components, we were able to identify possible dissociation pathways[30,31]. Our

114 prediction of possible stable oligomers using the PISA (Proteins, Interfaces, Surfaces

115 and Assemblies)[32] tool returned only the subunit dimer and icositetramer as stable

116 states (Table S1). We then used single value decomposition (SVD) to determine how

117 many components contribute to the observed variation in the pressure dissociation

118 SAXS data (Figure S1 and S2), and then fitted the dataset using various combinations

119 of oligomer structures derived from the ABfr icositetramer (Table S2, Figure S3 and

120 S4). The SVD analysis indicated two or three major components, with the three most

121 significant accounting for 93.5% of the total contributions (Figure S2). Two component

122 models consisting of the icositetramer and a subunit oligomer provided the worst fits

123    of the dataset (Table S3, Figure S5), though of these, the model consisting of the

124    icositetramer and dimer best represented the data. Three component models

125    generally provided better representations of the dissociation dataset (Figure S5), and

126    all models in which the dimer was the lowest oligomeric state gave the best fit quality.

127    Thus, in this pressure range, we assigned the initial and final state as icositetramer

128    and dimer. Ultimately, we found that the data were best represented by models

129    comprised of icositetramer, dimer and an intermediate hexamer, octamer or

130    dodecamer (Figure 1e). We acknowledge that there is no justification for selecting a

131    specific intermediate state based on these data alone, and therefore refrain from doing

132    so; the equivalence of the models and lack of cooperativity suggests that a range of

133    intermediate states are present during dissociation. Although little work has been

134    carried out on pressure-induced ferritin dissociation, there are many studies detailing

135    pH and denaturant-induced dissociation and reassembly of mammalian ferritin[33–38].

136    The dissociation products and mechanisms of reassociation observed are consistent

137    with the results obtained here, with dissociation to subunit dimer and reassociation *via*

138    intermediate species including tetramers, hexamers and octamers most commonly

139    reported.

140

141    To assess the effect of pressure on the internal structure, secondary structure and

142    folding of ABfr, we used a combination of Kratky analysis and high pressure

143    synchrotron radiation circular dichroism (CD). At low pressure, the Kratky plots for ABfr

144    exhibit multiple peaks that converge to baseline indicative of a globular, spherical

145    particle (Figure 1b). However, at pressures above 375 MPa, the Kratky plots

146    demonstrate a transitioning of ABfr from a spherical particle to a partially folded

147    structure. This may alter tertiary structure and interfacial interactions, destabilising the

148    icositetramer. We observed no significant change in the CD spectra between 0.1 MPa

149    and experimental limit of this technique, 200 MPa (Figure 1f), and predicted structural

150    composition *via* basis spectra remained constant (alpha helix = 0.99, beta sheet,

151    0.01)[39]. The CD data support the SAXS data in this pressure range, and it is therefore

152    likely that the observed changes in quaternary structure up to 375 MPa are due to the

153    system shifting towards a lower volume state, rather than significant perturbation of

154    the ABfr secondary structure[40].

155

156    We then explored the reversibility of the pressure dissociation process. Initially, ABfr

157    in 45 mM sodium phosphate (NaPi) buffer was pressurised to 450 MPa and held for 5

158    minutes before pressure release (Figure 2a). An immediate depression in $R_g$ was

159    observed, and the hollow spherical structure was lost after 30 seconds. Fitting the

160    change in icositetramer volume fraction against time with a single exponential function

161    (Figure S6), the observed rate constant ($k_{diss}$) of dissociation was determined to be

162    0.114 ± 0.002 s$^{-1}$. Almost complete reassembly occurred over 30 minutes following

163    depressurisation, as apparent from the recovery of the radius of gyration over time

164    (Figure 2a) and the hollow cage form of the P(r) function (Figure 2b). Again, fitting the

165    change in icositetramer volume fraction against time with a single exponential function,

166    the observed rate constant of reassociation ($k_{ass}$), was determined to be 0.006 ± 0.001

167    s$^{-1}$ (Figure S6). Following reassociation, we noted that the final $R_g$ and $I(0)$ values were

168    slightly lower than initial values (Figure 2a, b). To quantify the degree of reassociation

169    and to control for possible radiation damage or background mismatch, a sample of

170    ABfr in NaPi buffer (45 mM, pH 7) was pressurised under identical conditions without

171    SAXS measurement. Analytical ultracentrifugation (AUC) before pressurisation

172    (Figure 2c, Table S4) demonstrated that ABfr is fully assembled as the icositetramer

173    ($S_{20,\,w}$ = 15.76, MW = 424 kDa). Following pressurisation (t = 60 minutes), 94.3% of

174    ABfr was assembled in the icositetramer state ($S_{20,\,w}$ = 16.1, MW = 426 kDa), with the

175    remaining material present as the subunit dimer ($S_{20,\,w}$ = 3.53, MW = 44.5 kDa). TEM

176    imaging confirmed the presence of assembled ABfr cages both before and after

177    pressurisation, with no apparent change in morphology (Figure 2d, e).

178

179    The rate of reassociation under these conditions appears slow, and is significantly

180    slower than the calculated dimer collisional frequency[41] ($f_{25°C}$ = 6.79 x$10^5$ $S^{-1}$ at 25°C)

181    demonstrating unequivocally that reassembly is not diffusion limited. To test whether

182    recovery from pressure induced conformational drift influenced the kinetics of

183    reassociation[42,43], we assessed the degree of protein denaturation by inspection of a

184    normalised Kratky plot (Figure 2f), in which globular protein exhibits a maximum value

185    of 1.104 for $qR_g=\sqrt{3}$, whilst unfolded protein has a maximum value of 1.5-2[44]. This plot

186    confirmed that the protein recovers almost immediately from the denatured state after

187    pressure release, so the process is unlikely to be refolding-mediated.

188

189    The relatively slow rate of association may also be due to a kinetic barrier in the

190    association process which could arise from repulsive interactions between subunit

191    dimers. To determine the types of interaction dominant in this process, we explored

192    the effect of ionic strength and temperature on the nanocage reassembly, finding

193    strong correlation between these parameters and the rate and completeness of

194    nanocage reassembly (Figure 3, Table S5). We observed the most efficient

195    reassembly in high ionic strength sodium phosphate buffer (45 mM, 250 mM NaCl, pH

196    7; I = 373 mM)), with higher initial $R_g$ than the low ionic strength buffers and almost

197    complete reassembly at both 5 and 25 °C. In contrast, the assembly was notably

198   slower and less complete in lower ionic strength sodium phosphate buffer (pH 7, 45

199   mM; I = 123 mM) at both temperatures, with only gradual recovery of $R_g$ over the 1500

200   seconds of measurement. Most notably, the reassembly process in water was

201   significantly impaired at 25 °C, and was effectively arrested at 5 °C, with no

202   discernable increase in $R_g$ observed over 1500 seconds, indicating the presence of

203   only discrete subunit dimers within this timeframe. Given these data, we propose that

204   the reassembly of ABfr nanocages is likely driven by hydrophobic dispersion forces

205   while opposed by coulombic repulsion.

206

207   Similar ionic strength dependencies on nanocage reassembly were observed for the

208   naturally heme-free *E. coli* ferritin FtnA[45] following low pH-induced dissociation, and it

209   is likely that the origin of this effect lies at the interface between ferritin subunit dimers,

210   which associate to form the highly charged, carboxylate-rich ion channels at the C3

211   and C4 interfaces[46–48]. The increased degree and rate of reassembly with temperature

212   is a strong indication that assembly is entropically driven by the formation of weak

213   protein-protein interactions[49]. For oligomeric assemblies, the enthalpic contribution

214   ($\Delta H$) is generally small, because the strength of protein-water and water-water

215   interactions are similar. As such, increasing temperature decreases the Gibb's free

216   energy of association ($\Delta G^{ass}$ ) and favours assembly.

217

218   We also observed a greater degree of dissociation following pressurization at 5°C (5

219   minutes at 450 MPa) at all ionic strengths tested here; previous studies of pressure-

220   induced viral capsid dissociation have reported similar effects, and were attributed to

221   a strong entropic contribution to the free energy of association[50].  In these cases,

222   higher temperatures lower $\Delta G^{ass}$, promoting association in systems where entropic

223  contributions to the free energy dominate. Once the interfacial protein-protein

224  interactions (principally salt bridges and dispersion interactions) are broken and the

225  oligomers dissociate, dipole-dipole protein-water interactions are formed in their

226  place[50,51]. At high pressure, inherently shorter dipole interactions are favoured over

227  dispersion interactions due to the differential effect of compression on bond strength,

228  and dissociation occurs due to the increasing formation of protein-water interactions.

229  In addition, the hydration of hydrophobic surfaces is more favourable at high pressure,

230  as the ordered solvation shell is denser than the bulk solvent. Both similar and

231  contrasting behaviours have been reported for viral capsids under pressure. Silva *et*

232  *al.*[52,53] demonstrated that the 86-subunit bromegrass mosaic virus capsid undergoes

233  a reversible partial dissociation into dimers upon application of pressure (10 %

234  dissociation at 200 MPa). In contrast, the turnip yellow mosaic virus irreversibly

235  decapsidates rather than dissociates under pressure, resulting loss of RNA and

236  formation of a holed capsid, as the subunit interface contains few pressure sensitive

237  salt bridge and is rich in pressure insensitive hydrogen bonding interactions[54].

238

239  We subsequently investigated the ability of the native heme B prosthetic group to

240  modulate cage stability. Using a well-established procedure for tetrapyrrole extraction,

241  we removed heme B using an acidified water:2-butanone mixture and confirmed the

242  successful removal by UV/visible spectroscopy (Figure 4a)[55]. We next explored the

243  composition of oligomeric species in this apo-apo-Bfr (AABfr) by sedimentation

244  velocity analytical ultracentrifugation (SV-AUC, Figure 4b). In contrast to the heme

245  containing ABfr, the SV-AUC distribution reveals a mixture of assembled icositetramer

246  ($S_{(20, w)}$ = 15.85, MW = 427.1 kDa, 62.1%) and subunit dimer ($S_{(20, w)}$ = 2.97, MW =

247  34.7 kDa, 37.9%). The icositetramer peak is broadened, indicating greater

248    polydispersity and potentially incomplete assembly. We further characterized this

249    mixture of species by high-performance liquid chromatography-SAXS (HPLC-SAXS)

250    (Figure 4c), and observed scattering patterns consistent with both the assembled

251    icositetrameric nanocage ($R_g$ = 49.88 Å), and a smaller ellipsoidal or parallelepipedal

252    particle[56]. The extrapolated $R_g$ (22.21 Å) of the smaller particle is in good agreement

253    with that calculated for the subunit dimer (PDBID: 2VXI, $R_g$ = 21.16 Å)[57], and the Kratky

254    plot (Figure 4d) indicates a compact structure, although with a greater degree of

255    disorder than the AABfr icositetramer. We used bead modelling to analyse the SAXS

256    data for both the ABfr and AABfr icositetramers and found excellent agreement

257    between the hollow spherical models and the published Bfr crystal structure (Figure

258    4e)[57]. Similarly, the bead model of the AABfr subunit dimer closely overlays with the

259    crystal structure of the AABfr dimer (PDBID: 4CVP)[58]. To further probe the effects of

260    removing heme B from the nanocages, we used circular dichroism spectroscopy to

261    determine the thermal stabilities of the Bfr samples. We found the denaturation

262    midpoints of ABfr ($T_m$ = 68°C) and AABfr ($T_m$ = 58°C) in agreement with previously

263    reported values[59,60], confirming that removal of heme B has an overall destabilizing

264    effect on the protein. Comparison of the ABfr and AAbfr subunit dimer crystal

265    structures reveals slight secondary and tertiary structure differences that may impact

266    the ability of the dimer to assemble into the icositetramer (Figure S7). In particular, the

267    position of the E helix is shifted in the heme free protein; this helix lies at the

268    tetramerization interface and is essential for cage assembly (Figure S8)[61].

269

270    These data indicate that the binding of heme B not only leads to an increase in thermal

271    stability of the bulk Bfr protein, but it specifically stabilises the nanocage assembly.

272    While such increases in thermal stability induced through cofactor binding in heme-

273   proteins are widely reported, the bound cofactor's impact on cage stability and

274   assembly is unknown[62]. To determine the effect of heme B on the pressure stability of

275   Bfr, we pressurised AABfr to 450 MPa in 25 MPa increments, allowing time at each

276   step for equilibration before SAXS measurement (Figure 5a). We found the real space

277   distribution for ABfr at ambient pressure is representative of a mixture of assembled

278   icositetramers and smaller subunit oligomers, in good agreement with the SV-AUC

279   data described above (Figure 5b). The icositetramer nanocage structure visible in the

280   real space distribution is rapidly lost with applied pressure, whilst the final state

281   resembles a mixture of the subunit dimer and other lower order oligomers. The Kratky

282   plots demonstrate a less globular structure than ABfr at similar pressures, and do not

283   reveal any further unfolding over the pressure range (Figure 5c). The initial $R_g$ for

284   AABfr (42 Å) Is notably lower than that of ABfr (50 Å) due to the mixture of icositetramer

285   and dimer at ambient pressure. The $R_g$ remains constant until 175 MPa, then

286   deceases, reaching a plateau at 350 MPa, demonstrating that AABfr is significantly

287   less pressure stable than ABfr (Figure 5d). The final $R_g$ of 35 Å, was higher than that

288   of ABfr (32 Å), suggesting a dissociation endpoint with a different oligomeric state.

289

290 **Conclusions**

291 We have demonstrated here that hydrostatic pressure is a valuable method to control

292 and modulate the assembly, disassembly and oligomeric composition of the

293 bacterioferritin nanocage. It is highly likely that this methodology can be extended to

294 other protein nanocages, especially those stabilized primarily by hydrophobic

295 interactions. Since the method we report here is also gentle, tunable and not limited

296 to intrinsically metastable or mutationally compromised cages, more robust hybrid

297 materials tolerant of harsh environmental conditions are potentially accessible. Full

298 cage dissociation might also provide a route to higher loading ratios of therapeutic

299 molecules or larger payloads unable to traverse the protein cage, leading, for example,

300 to significantly improved synthetic routes to nanocage-based drug delivery vehicles.

301

302 Furthermore, we have also demonstrated that the heme B prosthetic groups

303 significantly enhance the Bfr nanocage stability. While it has been previously reported

304 that heme B facilitates electron transfer and iron release from the Bfr core, this can

305 occur in the absence of the prosthetic group and it is notable that heme B is absent in

306 many/most of the known ferritins. It therefore seems plausible that an additional major

307 role of heme B in Bfr is to stabilise the protein nanocage, thus enabling the retention

308 of the protein superstructure for iron mineralisation.

309

310 **Methods**

311 **Protein expression and purification**

312 Bacterioferritin expression was carried out in T7 express *E. coli* BL21 (DE3) cells using

313 a modified pUC119 plasmid, PGS281 as described in Andrews *et al*[63]. Cultures were

314 grown aerobically at 37 °C in LB media containing 34 µg mL$^{-1}$ carbenicillin. Flasks

315 were shaken for 24 hours at 200 rpm, before cultures were harvested by centrifugation

316 (10 minutes, 7277 ×g rcf). The pellets were washed then re-suspended in lysis buffer

317 (1.5 mM $KH_2PO_4$, 8 mM $Na_2HPO_4$, 150 mM NaCl, 3 mM KCl, pH 7).

318 Phenylmethylsulfonyl fluoride (PMSF) (1 mM) was added, and then cells were lysed

319 using a probe sonicator (3 × 20s, maximum amplitude). The crude extract was then

320 centrifuged (47808 ×g, 60 minutes). The supernatant was decanted, heated to 70 °C

321 for 15 minutes, then cooled and centrifuged (47808 ×g, 30 minutes). The supernatant

322 was concentrated using a centrifugal concentrator (MWCO = 50 kDa) to half the

323 original volume. The extract was purified by size exclusion chromatography using a

324 Sephadex S200 26/600 column equilibrated with lysis buffer at a flow rate of 2.3 mL

325 *per* minute. Bfr containing fractions were pooled, concentrated, and then further

326 purified by anion exchange chromatography using a Q-Sepharose FF column. The

327 target protein was eluted with a linear gradient of 0-0.3 M NaCl in histidine buffer (20

328 mM histidine.HCl, pH 5.5). The purified protein was dialysed in a solution of EDTA (10

329 mM) and DTT (5 mM) to remove the native core, forming ABfr.

330

331 **High pressure SAXS measurement**

332 Data collection was carried out at the I22 beamline, Diamond Light Source (DLS,

333 Harwell, UK), using a hydrostatic pressure cell with a maximum operation pressure of

334 500 MPa[28]. Samples were loaded into thin-wall polycarbonate capillaries (θ=2 mm),

335    which were then sealed with a rubber bung and two-part adhesive. The beam energy

336    was 18 keV ($\lambda$ = 0.69 Å) to reduce absorption from the diamond windows and water in

337    the beam path. ABfr samples were prepared at a concentration of 5 mg mL$^{-1}$ in a range

338    of buffers and centrifuged (10 minutes, 16000 ×g) prior to measurement. The collection

339    time for individual measurements was between 6 and 60 s. Hydrostatic pressure

340    experiments were performed under both equilibrium and dynamic, time resolved

341    conditions. In the former, the pressure was raised in incremental steps allowing time

342    for equilibrium before measurement. The beam was blocked during equilibration to

343    prevent radiation damage. In dynamic experiments the sample was pressurised, held

344    at pressure, then returned to ambient pressure whilst measuring the time resolved

345    scattering pattern. Pressure jump experiments were conducted in which pressure was

346    increased rapidly to 450 MPa whilst measuring the time resolved scattering. The data

347    were collected using a Pilatus P3-2M detector. The sample to detector distance was

348    6 m, providing a $q$-range of 0.008-0.52 Å$^{-1}$. The two-dimensional data sets were

349    reduced using DAWN[64]. Briefly, the $q$-axis was calibrated using with a silver behenate

350    standard data, then detector images were masked, radially averaged from the beam

351    centre and normalised to absolute intensity using a glassy carbon standard.

352    Background subtraction was carried out using a user-written python script (Figure S9

353    and S10) to account for background mismatch in the high-$q$ data region. This

354    mismatch resulted from the necessity of using different capillaries for sample and

355    background, and slight changes in cell and capillary position when changing samples.

356    Whilst this mismatch was generally low, systemic under-subtraction at low pressure

357    and over-subtraction at high pressure was present across data sets. The background

358    measurement was multiplied by a constant to align the high-$q$ region with that of the

359    sample. The median I($q$) of the region $q$ = 0.3-0.4 Å$^{-1}$ was determined for both sample

360 and background data. The background was then multiplied by a constant, $k$, such that

361 the corrected median $I(q)$ of the background was equal to the median $I(q)$ of the sample

362 minus a small constant, $A$. The scaling constant was therefore:

363

364 $$k = \frac{I(q)_{sample} - A}{I(q)_{background}} \qquad q = 0.3 - 0.4\,\text{Å}^{-1}$$

365 This method was effective in background matching the high-$q$ data region and

366 preventing over and under subtraction with $k = 1 \times 10^{-5}$. Example data corrections for

367 ABfr at 0.1 MPa and 200 MPa are shown in Figure S9. The background adjustment

368 results in lower overall $I(q)$ relative to the unprocessed data, but the shape of the

369 scattering curve is preserved. Artefacts resulting from Kossel lines are visible in the

370 data at 200 MPa at $q = 0.016$ and $0.7\,\text{Å}^{-1}$ despite background subtraction. The effect

371 is most visible in the 2D detector image, shown in Figure S10. Kossel lines are

372 observed between 100-300 MPa in both background and sample images. The

373 intensity of the effect is pressure dependent, and line position is dependent on the

374 orientation of the diamond windows. Care was taken to repeat background

375 measurements following window changes. However, mismatched line intensity

376 between sample and background resulted in artefacts in the reduced data. The

377 mismatch occurs due to the pressure dependence of line intensity: whilst pressure

378 control is accurate to 0.1 MPa in this apparatus, slight pressure loss often occurs

379 during measurement due to leakage. Consequently, pressure differences between

380 samples and background measurements of up to 0.3 MPa are observed. Although

381 visible in the data, the artefacts are small and not expected to affect subsequent fitting

382 and data analysis. Parasitic scattering is present in some data sets, particularly where

383 Kossel lines intersect with the beam-stop (Figure S10 (200 MPa)). This effect is not

384 effectively removed by background subtraction, and manifests as aggregation-like

385 scattering at $q < 0.04$ Å$^{-1}$, which precludes the use of Guinier methods for the

386 approximation of I(0) and $R_g$, but does not affect the determination of these parameters

387 from the indirect Fourier transform of the data.

388

389 **High pressure liquid chromatography small angle X-ray scattering**

390 HPLC-SAXS measurements were carried out using the B21 beamline at the Diamond

391 Light Source, Harwell, UK. Measurements were taken with a camera length of 3.9 m

392 and a beam energy of 12.4 keV. The beam cross section was 1 x 5 mm. The scattering

393 angle and absolute intensity were pre-calibrated using silver behenate and glassy

394 carbon standards. Samples were measured in a glass capillary at a concentration of

395 2-5 mg mL$^{-1}$ and a temperature of 25°C. Data were collected in 30 successive frames

396 of one second each. Inline HPLC separation was carried out using a Shodex KW 403

397 column. The 2D SAXS patterns obtained were radially averaged from the beam centre,

398 normalised to an absolute intensity scale using a glassy carbon standard and

399 corrected for background scattering from buffer components. ScÅtter was used to

400 determine basic SAXS invariants and determine the pair distance distribution (P(r))

401 functions from the experimental data as described previously[65,66]. Ab initio modelling

402 was carried out using DAMMIF and DAMAVER with no symmetry restrictions[67]. The

403 crystallographic model of *E. coli* bacterioferritin was obtained from the Protein Data

404 Bank (PDB code: 2VXI, 4CVP), and aligned to the reconstructed structural models

405 using the program SUPALM[68].

406

407

408

**Circular Dichroism**

Circular dichroism (CD) spectroscopy was used to determine the relative thermal stabilities of ABfr and AABfr and to investigate the secondary structure of both proteins. Solutions of ABfr or AABfr (0.5 g $L^{-1}$) were prepared in 45 mM sodium phosphate buffer (pH 7). The far UV spectrum (190-260 nm) was measured at 25 °C, then the temperature was increased in 3 degree increments allowing for equilibration (300s) at each step. The helical content was measured by monitoring mean residue ellipticity at $\lambda$= 222 nm. The thermal denaturation midpoint temperature was determined using sigmoidal fits of the raw the $[\theta_{222\ nm}]$ data and from the maxima in first differential of the $[\theta_{222\ nm}]$ data (Figure 4f). Secondary structure composition was determined by linear combination of basis spectra using CAPITO[39].

**High pressure circular dichroism**

High pressure circular dichroism measurements were carried out at the B23 beamline, Diamond Light Source (DLS, Harwell, UK), using a hydrostatic pressure cell with a maximum operation pressure of 200 MPa[69]. Results obtained were processed using CDApps and OriginLab. Secondary structure estimation from CD spectra was carried out using the CAPITO CD analysis and plotting tool[39].

**Sedimentation velocity analytical ultracentrifugation**

Sedimentation velocity was measured in sodium phosphate buffer (45 mM NaPi, 250 mM NaCl, pH 7) using a Beckmann ProteomeLab XL-I at 20 ° C and 24000 rpm. Data were collected at a wavelength of 418 nm. Date file time stamps were corrected using REDATE, and continuous sedimentation velocity coefficient (c(S)) distributions were produced using SEDFIT. Buffer density and viscosity were measured using an Anton-

434    Paar rolling ball viscometer. The protein partial specific volume was calculated from

435    the primary sequence ($\tilde{v}$ = 0.736 cm$^3$ g$^{-1}$).

436

**Transmission electron microscopy**

438    All transmission electron microscopy data were collected by using a JEOL 1200 MK2

439    TEM at the University of Bristol. Bfr samples were deposited onto carbon film coated

440    copper mesh grids and stained using phosphotungstic acid, which is not internalised

441    by the protein cage.

442

**PISA analysis of ABfr**

444    A bioinformatics approach was adopted in order to identify potential dissociation states

445    of ABfr under pressure. The Proteins, Interfaces, Structures and Assemblies (PISA)

446    tool was used to calculate overall solvent accessible surface areas, solvation free

447    energies ($\Delta G^{int}$) and dissociation free energies ($\Delta G^{diss}$) for stable subunit oligomers of

448    ABfr[32,70,71]. The PISA analysis identifies thermodynamically stable assemblies of

449    subunits based on interfacial interactions. For ABfr, only the fully assembled

450    icositetramer and dimer were identified as stable quaternary structures in solution. The

451    surface areas and free energies of these species are shown in Table S1. The free

452    energy of dissociation, $\Delta G^{diss}$, corresponds to the free energy difference between

453    associated and dissociated states. A positive value indicates that the assembled state

454    is stable under standard conditions.

455

**SVD analysis and oligomer model fitting of ABfr pressure dissociation.**

457    SVDPLOT and Ultrascan II were used to produce a set of basis eigenvectors and

458    eigenvalues for the ABfr dataset (Figure S1)[31,72]. A non-parameterised runs test was

459    used to identify non-random curves in the eigenvector set[73]. Eigenvectors with $p <$

460    0.05 were deemed to be non-random, yielding 12 significant eigenvectors. Inspection

461    of the ABfr eigenvectors revealed that those with the highest three eigenvalues are

462    smooth curves reminiscent of scattering form factors, and so are likely to contain

463    structural information corresponding to the initial icositetramer and oligomeric

464    dissociation products. The subsequent curves are structured, but contain significant

465    noise, and may contain contributions from minor species as well as background

466    components due to path length variation an imperfect background subtraction. The

467    data were then reconstructed incrementally by adding eigenvectors to the model in

468    order of decreasing significance. The root mean squared deviation between the

469    reconstructed datasets and the experimental curves was calculated at each stage

470    (Figure S2).

471

472    Subunit oligomer models were extracted from the crystal structure of the full ABfr

473    icositetramer (2VXI), and theoretical scattering data from these models was calculated

474    using CRYSOL (Figures S3 and S4)[30]. OLIGOMER was then used to fit linear

475    combinations of these oligomers to the experimental dataset[31]. Fit quality was

476    assessed by the reduced chi-squared value and by inspection of fit residuals (Figure

477    S5 and Table S3).

478

479

**Author Contributions**

J.L.R.A and A.W.P conceived the project; K.L.V., D.W., B.C., D.T., V.T., and A.J.S. performed the experiments; K.L.V., B.C., H.C., R.R., A.J.S., J.L.R.A. and A.W.P. discussed the results; K.L.V. and J.L.R.A. wrote the manuscript.

**Supporting Information**

PISA analysis, detailed AUC data, structural models and additional SAXS data including single value decomposition, calculated P(r) distributions, OLIGOMER models, ABfr dissociation data and background subtraction examples are provided in the supporting information.

## References

1. Bhaskar, S. & Lim, S. Engineering protein nanocages as carriers for biomedical applications. *NPG Asia Materials* **9**, e371–e371 (2017).

2. Kanekiyo, M. *et al.* Self-assembling influenza nanoparticle vaccines elicit broadly neutralizing H1N1 antibodies. *Nature* **499**, 102–106 (2013).

3. Ren, H., Zhu, S. & Zheng, G. Nanoreactor design based on self-assembling protein nanocages. *Int. J. Mol. Sci.* **20**, (2019).

4. Maity, B., Fujita, K. & Ueno, T. Use of the confined spaces of apo-ferritin and virus capsids as nanoreactors for catalytic reactions. *Curr. Opin. Chem. Biol.* **25**, 88–97 (2015).

5. Douglas, T. & Stark, V. T. Nanophase cobalt oxyhydroxide mineral synthesized within the protein cage of ferritin. *Inorg. Chem.* **39**, 1828–1830 (2000).

6. Yamashita, I., Hayashi, J. & Hara, M. Bio-template Synthesis of Uniform CdSe Nanoparticles Using Cage-shaped Protein, Apoferritin. *Chem. Lett.* **33**, 1158–1159 (2004).

7. Ueno, T. *et al.* Size-selective olefin hydrogenation by a Pd nanocluster provided in an apo-ferritin cage. *Angew. Chemie - Int. Ed.* **43**, 2527–2530 (2004).

8. Douglas, T. *et al.* Protein engineering of a viral cage for constrained nanomaterials synthesis. *Adv. Mater.* **14**, 415–418 (2002).

9. He, D. & Marles-Wright, J. Ferritin family proteins and their use in bionanotechnology. *N. Biotechnol.* **32**, 651–657 (2015).

10. Jutz, G., Van Rijn, P., Santos Miranda, B. & Böker, A. Ferritin: A versatile building block for bionanotechnology. *Chem. Rev.* **115**, 1653–1701 (2015).

11. Putri, R. M. *et al.* Structural Characterization of Native and Modified Encapsulins as Nanoplatforms for in Vitro Catalysis and Cellular Uptake. *ACS Nano* **11**,

522         12796–12804 (2017).

523    12.    Choi, S. H., Kwon, I. C., Hwang, K. Y., Kim, I. S. & Ahn, H. J. Small heat shock protein as a multifunctional scaffold: Integrated tumor targeting and caspase imaging within a single cage. *Biomacromolecules* **12**, 3099–3106 (2011).

526    13.    Azuma, Y., Edwardson, T. G. W. & Hilvert, D. Tailoring lumazine synthase assemblies for bionanotechnology. *Chemical Society Reviews* **47**, 3543–3557 (2018).

529    14.    Butterfield, G. L. *et al.* Evolution of a designed protein assembly encapsulating its own RNA genome. *Nature* **552**, 415–420 (2017).

531    15.    Malay, A. D. *et al.* An ultra-stable gold-coordinated protein cage displaying reversible assembly. *Nature* **569**, 438–442 (2019).

533    16.    Swift, J., Butts, C. A., Cheung-Lau, J., Yerubandi, V. & Dmochowski, I. J. Efficient Self-Assembly of Archaeoglobus fulgidus ferritin around metallic cores. *Langmuir* **25**, 5219–5225 (2009).

536    17.    Sana, B., Johnson, E. & Lim, S. The unique self-assembly/disassembly property of Archaeoglobus fulgidus ferritin and its implications on molecular release from the protein cage. *Biochim. Biophys. Acta - Gen. Subj.* **1850**, 2544–2551 (2015).

539    18.    Nasrollahi, F. *et al.* Incorporation of Graphene Quantum Dots, Iron, and Doxorubicin in/on Ferritin Nanocages for Bimodal Imaging and Drug Delivery. *Adv. Ther.* **3**, 1900183 (2020).

542    19.    Fletcher, J. M. *et al.* Self-assembling cages from coiled-coil peptide modules. *Science (80-. ).* **340**, 595–599 (2013).

544    20.    Peng, T. & Lim, S. Trimer-based design of pH-responsive protein cage results in soluble disassembled structures. *Biomacromolecules* **12**, 3131–3138 (2011).

546    21.    Dalmau, M., Lim, S. & Wang, S. W. Design of a pH-dependent molecular switch

547          in a caged protein platform. *Nano Lett.* **9**, 160–166 (2009).

548    22.   Pontillo, N., Pane, F., Messori, L., Amoresano, A. & Merlino, A. Cisplatin

549          encapsulation within a ferritin nanocage: A high-resolution crystallographic

550          study. *Chem. Commun.* **52**, 4136–4139 (2016).

551    23.   Liu, X. *et al.* Apoferritin-CeO2nano-truffle that has excellent artificial redox

552          enzyme activity. *Chem. Commun.* **48**, 3155–3157 (2012).

553    24.   Skouri-Panet, F., Quevillon-Cheruel, S., Michiel, M., Tardieu, A. & Finet, S.

554          sHSPs under temperature and pressure: The opposite behaviour of lens alpha-

555          crystallins and yeast HSP26. *Biochim. Biophys. Acta - Proteins Proteomics*

556          **1764**, 372–383 (2006).

557    25.   White, H. E. *et al.* Multiple Distinct Assemblies Reveal Conformational Flexibility

558          in the Small Heat Shock Protein Hsp26. *Structure* **14**, 1197–1204 (2006).

559    26.   Zhang, T. *et al.* Effect of high hydrostatic pressure (HHP) on structure and

560          activity of phytoferritin. *Food Chem.* **130**, 273–278 (2012).

561    27.   Wang, Q. *et al.* High hydrostatic pressure encapsulation of doxorubicin in ferritin

562          nanocages with enhanced efficiency. *J. Biotechnol.* **254**, 34–42 (2017).

563    28.   Brooks, N. J. *et al.* Automated high pressure cell for pressure jump x-ray

564          diffraction. *Rev. Sci. Instrum.* **81**, 064103 (2010).

565    29.   Tanner, J. J. Empirical power laws for the radii of gyration of protein oligomers.

566          *Acta Crystallogr. Sect. D Struct. Biol.* **72**, 1119–1129 (2016).

567    30.   Svergun, D., Barberato, C. & Koch, M. H. CRYSOL - A program to evaluate X-

568          ray solution scattering of biological macromolecules from atomic coordinates. *J.*

569          *Appl. Crystallogr.* **28**, 768–773 (1995).

570    31.   Konarev, P. V., Volkov, V. V., Sokolova, A. V., Koch, M. H. J. & Svergun, D. I.

571          PRIMUS: A Windows PC-based system for small-angle scattering data analysis.

572            *J. Appl. Crystallogr.* **36**, 1277–1282 (2003).

573    32.    Krissinel, E. & Henrick, K. Inference of Macromolecular Assemblies from

574            Crystalline State. *J. Mol. Biol.* **372**, 774–797 (2007).

575    33.    Stefanini, S., Vecchini, P. & Chiancone, E. On the Mechanism of Horse Spleen

576            Apoferritin Assembly: A Sedimentation Velocity and Circular Dichroism Study.

577            *Biochemistry* **26**, 1831–1837 (1987).

578    34.    Gerl, M. & Jaenicke, R. Mechanism of the self-assembly of apoferritin from horse

579            spleen - Cross-linking and spectroscopic analysis. *Eur. Biophys. J.* **15**, 103–109

580            (1987).

581    35.    Banyard, S. H., Stammers, D. K. & Harrison, P. M. Electron density map of

582            apoferritin at 2.8-Å resolution. *Nature* **271**, 282–284 (1978).

583    36.    Sato, D. *et al.* Ferritin Assembly Revisited: A Time-Resolved Small-Angle X-ray

584            Scattering Study. *Biochemistry* **55**, 287–293 (2016).

585    37.    Kilic, M. a, Spiro, S. & Moore, G. R. Stability of a 24-meric homopolymer:

586            comparative studies of assembly-defective mutants of Rhodobacter capsulatus

587            bacterioferritin and the native protein. *Protein Sci.* **12**, 1663–1674 (2003).

588    38.    Andrews, S. C. *et al.* Physical, chemical and immunological properties of the

589            bacterioferritins of Escherichia coli, Pseudomonas aeruginosa and Azotobacter

590            vinelandii. *Biochim. Biophys. Acta - Protein Struct. Mol. Enzymol.* **1078**, 111–

591            116 (1991).

592    39.    Wiedemann, C., Bellstedt, P. & Görlach, M. CAPITO - A web server-based

593            analysis and plotting tool for circular dichroism data. *Bioinformatics* **29**, 1750–

594            1757 (2013).

595    40.    Weber, G. Thermodynamics of the association and the pressure dissociation of

596            oligomeric proteins. *J. Phys. Chem.* **97**, 7108–7115 (1993).

597  41.  Atkins, P. & de, P. J. Atkins' Physical Chemistry, 7th Edition. *Oxford Univ. Press*

598       (2002).

599  42.  Ward, A. B., Sali, A. & Wilson, I. A. Integrative Structural Biology. *Science (80-.*

600       *).* **339**, 913–915 (2013).

601  43.  Brooks-Bartlett, J. C. *et al.* Development of tools to automate quantitative

602       analysis of radiation damage in SAXS experiments. *J. Synchrotron Radiat.* **24**,

603       63–72 (2017).

604  44.  Kikhney, A. G. & Svergun, D. I. A practical guide to small angle X-ray scattering

605       (SAXS) of flexible and intrinsically disordered proteins. *FEBS Lett.* **589**, 2570–

606       2577 (2015).

607  45.  Sato, D. *et al.* Electrostatic Repulsion during Ferritin Assembly and Its Screening

608       by Ions. *Biochemistry* **55**, 482–488 (2016).

609  46.  Watt, R. K., Hilton, R. J. & Graff, D. M. Oxido-reduction is not the only

610       mechanism allowing ions to traverse the ferritin protein shell. *Biochimica et*

611       *Biophysica Acta - General Subjects* **1800**, 745–759 (2010).

612  47.  Bakker, G. R. & Boyer, R. F. Iron incorporation into apoferritin. The role of

613       apoferritin as a ferroxidase. *J. Biol. Chem.* **261**, 13182–13185 (1986).

614  48.  Rui, H., Rivera, M. & Im, W. Protein dynamics and ion traffic in bacterioferritin.

615       *Biochemistry* **51**, 9900–9910 (2012).

616  49.  Kegel, W. K. & van der Schoot, P. Competing Hydrophobic and Screened-

617       Coulomb Interactions in Hepatitis B Virus Capsid Assembly. *Biophys. J.* **86**,

618       3905–3913 (2004).

619  50.  Silva, J. Pressure Stability of Proteins. *Annu. Rev. Phys. Chem.* **44**, 89–113

620       (1993).

621  51.  Silva, J. L., Foguel, D. & Royer, C. A. Pressure provides new insights into protein

622        folding, dynamics and structure. *Trends Biochem. Sci.* **26**, 612–618 (2001).

623   52.   Silva, J. L. & Weber, G. Pressure-induced dissociation of brome mosaic virus.

624        *J. Mol. Biol.* **199**, 149–159 (1988).

625   53.   Leimkühler, M., Goldbeck, A., Lechner, M. D. & Witz, J. Conformational changes

626        preceding decapsidation of bromegrass mosaic virus under hydrostatic

627        pressure: A small-angle neutron scattering study. *J. Mol. Biol.* **296**, 1295–1305

628        (2000).

629   54.   Leimkühler, M. *et al.* The formation of empty shells upon pressure induced

630        decapsidation of turnip yellow mosaic virus. *Arch. Virol.* **146**, 653–667 (2001).

631   55.   Teale, F. W. J. Cleavage of the haem-protein link by acid methylethylketone.

632        *BBA - Biochim. Biophys. Acta* **35**, 543 (1959).

633   56.   Nayuk, R. & Klaus, H. Formfactors of Hollow and Massive Rectangular

634        Parallelepipeds at Variable Degree of Anisometry. *Zeitschrift für Physikalische*

635        *Chemie* **226**, 837 (2012).

636   57.   Willies, S. C., Isupov, M. N., Garman, E. F. & Littlechild, J. A. The binding of

637        haem and zinc in the 1.9 Å X-ray structure of Escherichia coli bacterioferritin. *J.*

638        *Biol. Inorg. Chem.* **14**, 201–207 (2009).

639   58.   Hingorani, K. *et al.* Photo-oxidation of tyrosine in a bio-engineered

640        bacterioferritin 'reaction centre' - A protein model for artificial photosynthesis.

641        *Biochim. Biophys. Acta - Bioenerg.* **1837**, 1821–1834 (2014).

642   59.   Ardejani, M. S., Li, N. X. & Orner, B. P. Stabilization of a protein nanocage

643        through the plugging of a protein-protein interfacial water pocket. *Biochemistry*

644        **50**, 4029–4037 (2011).

645   60.   Wong, S. G. *et al.* Structural and mechanistic studies of a stabilized subunit

646        dimer variant of Escherichia coli bacterioferritin identify residues required for

647         core formation. *J. Biol. Chem.* **284**, 18873–18881 (2009).

648   61.   Fan, R., Boyle, A. L., Vee, V. C., See, L. N. & Orner, B. P. A helix swapping

649         study of two protein cages. *Biochemistry* **48**, 5623–5630 (2009).

650   62.   Hargrove, M. S. *et al.* Stability of Myoglobin: A Model for the Folding of Heme

651         Proteins. *Biochemistry* **33**, 11767–11775 (1994).

652   63.   Andrews, S. C. *et al.* Overproduction, purification and characterization of the

653         bacterioferritin of Escherichia coli and a C-terminally extended variant. *Eur. J.*

654         *Biochem.* **213**, 329–338 (1993).

655   64.   Basham, M. *et al.* Data Analysis WorkbeNch (DAWN). *J. Synchrotron Radiat.*

656         **22**, 853–858 (2015).

657   65.   Rambo, R. P. & Tainer, J. A. Accurate assessment of mass, models and

658         resolution by small-angle scattering. *Nature* **496**, 477–481 (2013).

659   66.   Rambo, R. P. & Tainer, J. A. Characterizing flexible and intrinsically unstructured

660         biological macromolecules by SAS using the Porod-Debye law. *Biopolymers* **95**,

661         559–571 (2011).

662   67.   Franke, D. & Svergun, D. I. DAMMIF, a program for rapid ab-initio shape

663         determination in small-angle scattering. *J. Appl. Crystallogr.* **42**, 342–346

664         (2009).

665   68.   Konarev, P. V., Petoukhov, M. V. & Svergun, D. I. Rapid automated

666         superposition of shapes and macromolecular models using spherical

667         harmonics. *J. Appl. Crystallogr.* **49**, 953–960 (2016).

668   69.   Hussain, R., Jávorfi, T. & Siligardi, G. Circular dichroism beamline B23 at the

669         Diamond Light Source. *J. Synchrotron Radiat.* **19**, 132–135 (2012).

670   70.   De Val, N., Declercq, J. P., Lim, C. K. & Crichton, R. R. Structural analysis of

671         haemin demetallation by L-chain apoferritins. *J. Inorg. Biochem.* **112**, 77–84

672    (2012).

673  71.  Chen, C. R. & Makhatadze, G. I. ProteinVolume: calculating molecular van der

674    Waals and void volumes in proteins. *BMC Bioinformatics* **16**, 101 (2015).

675  72.  Demeler, B. *et al.* Characterization of size, anisotropy, and density heterogeneity

676    of nanoparticles by sedimentation velocity. *Anal. Chem.* **86**, 7688–7695 (2014).

677  73.  Wald, A. & Wolfowitz, J. On a Test Whether Two Samples are from the Same

678    Population. *Ann. Math. Stat.* **11**, 147–162 (1940).

679  74.  Hansen, S. BayesApp: A web site for indirect transformation of small-angle

680    scattering data. *J. Appl. Crystallogr.* **45**, 566–567 (2012).

681

682
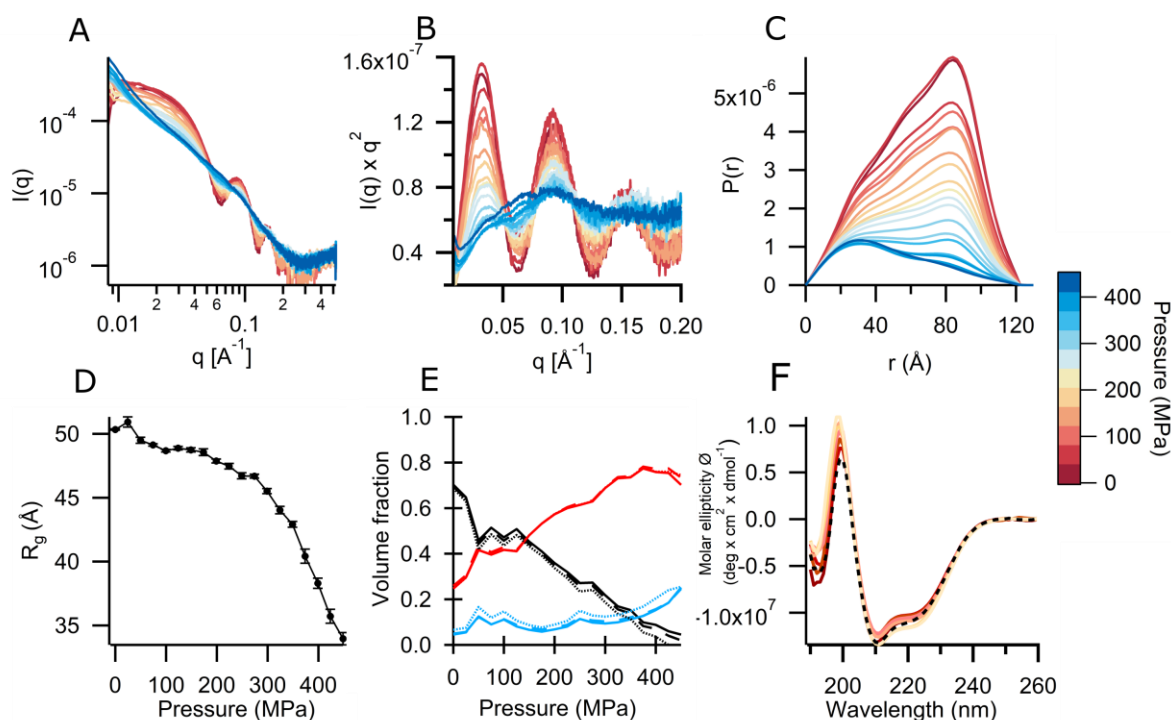
**Figure 1. Pressure dissociation of ABfr under equilibrium conditions between 0.1 and 450 MPa measured using high pressure synchrotron radiation SAXS and circular dichroism. (A)** Reciprocal space SAXS profiles, **(B)** Kratky plots, **(C)** pair distance distribution (P(r)) functions, **(D)** change in radius of gyration, $R_g$, with pressure, **(E)** change in solution oligomer composition with pressure and **(F)** circular dichroism spectra. SAXS data were collected between 0.1 MP (red) and 450 MPa (blue) at a protein concentration of 5 mg mL$^{-1}$ in 45 mM sodium phosphate buffer (pH 7). Real space transformations were performed using BAYESAPP, which uses Bayesian analysis to select parameters such as $D_{max}$ and data noise level.[74] I(0) and $R_g$ were calculated from real space data. I(0) was normalised to a maximum value of 1. Component volume fraction versus pressure generated from OLIGOMER models of ABfr dissociation. The volume fractions of the icositetramer, *n*-mer and dimer are shown in black, blue and red respectively. The intermediate oligomer states are hexamer (solid line), octamer (dashed line) and dodecamer (dotted line). High-pressure circular dichroism data was collected between 0.1 (red) and 200 MPa (yellow) at a protein concentration of 0.03 mg mL$^{-1}$, 45 mM sodium phosphate, pH 7.
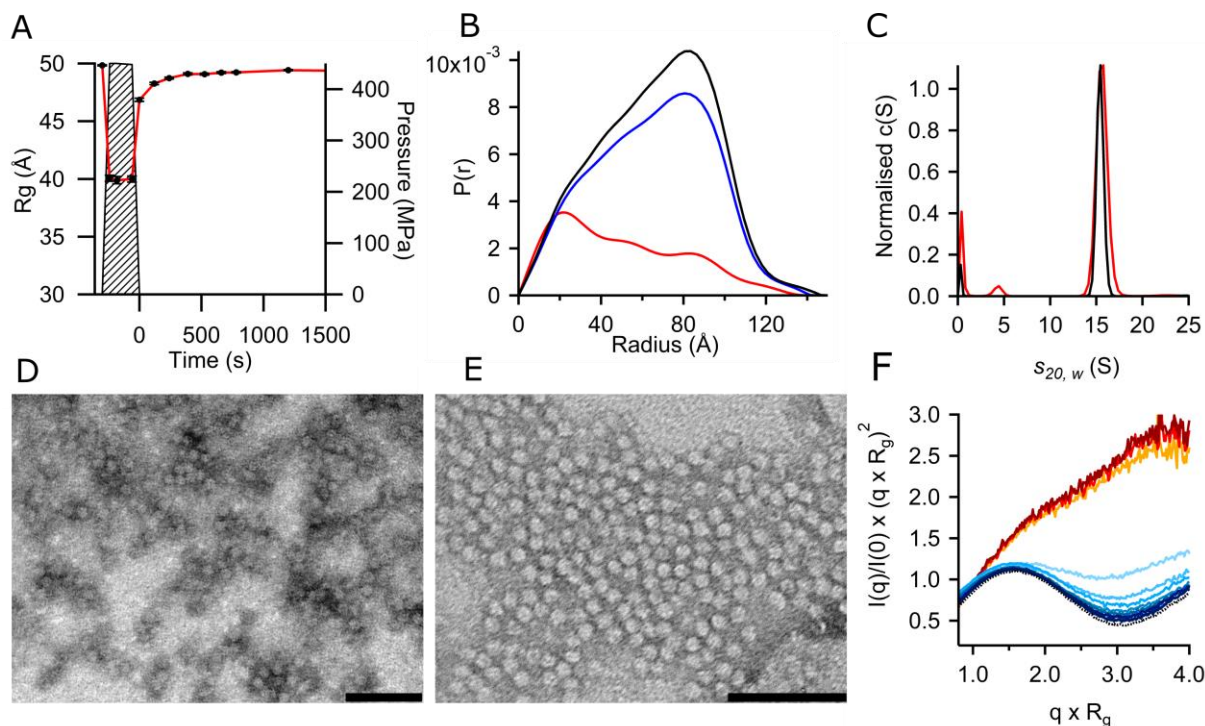
713
714 **Figure 2. Reassociation of ABfr following pressure induced dissociation measured by SAXS,**
715 **AUC and TEM. (A)** Changes in ABfr $R_g$ pre, during and post- pressurization measured by SAXS.
716 Pressure cycle was performed at 25°C NaPi (45 mM, pH 7, I = 123 mM). **(B)** Pair distance distribution
717 (P(r)) functions for ABfr pre- (black), during (red) and post- pressurisation (blue). **(C)** Sedimentation
718 velocity c(S) distribution for ABfr pre-pressurisation (black) and post-pressurisation (red). Sedimentation
719 velocity was measured at a protein concentration of approximately 50 µM in sodium phosphate buffer
720 (45 mM NaPi, 250 mM NaCl, pH 7) using a Beckmann ProteomeLab XL-I at 20°C and 24000 rpm. Data
721 was collected at a wavelength of 418 nm. Data file time stamps were corrected using REDATE, and
722 continuous sedimentation coefficient (c(S)) distributions were fitted using SEDFIT. Buffer density (ρ =
723 1.003 g cm-3) and viscosity (η = 1.0107 mPa s-1) were measured using an Anton-Paar rolling ball
724 viscometer. **(D)** Negative stain (phosphotungstic acid) TEM images of ABfr pre-pressurisation and **(E)**
725 and post-pressurisation (scale bars = 100 nm). **(F)** Change in normalised Kratky intensity
726 ($I_{(q=1.1)}/I_{(0)}$x($q*R_g$)$^2$) with pre, during and post- pressurization. Dotted black trace shows pre-
727 pressurisation data, yellow – red traces show pressurised data at 0, 120 and 300s, light blue – dark
728 blue traces show post pressurisation data with increasing time.
729
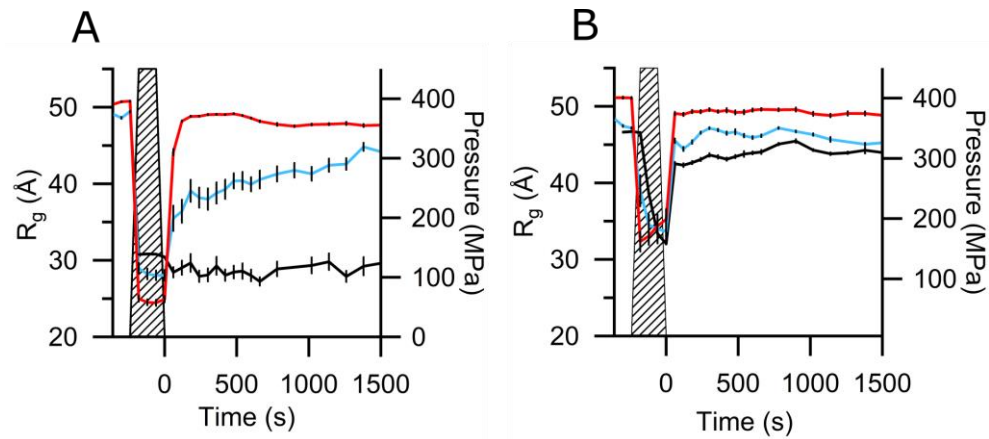
730
731 **Figure 3. Changes in ABfr $R_g$ pre, during and post- pressurisation.** Pressure cycles were performed
732 at 5 ˚C **(A)** and 25˚C **(B)** in $H_2O$ (I = 0 mM, black), NaPi (45 mM, pH 7, I = 123 mM, blue) and in NaPi
733 (45 mM, pH 7) + NaCl (250 mM) (I = 373 mM, red). Pressure level depicted as hashed region.
734

735
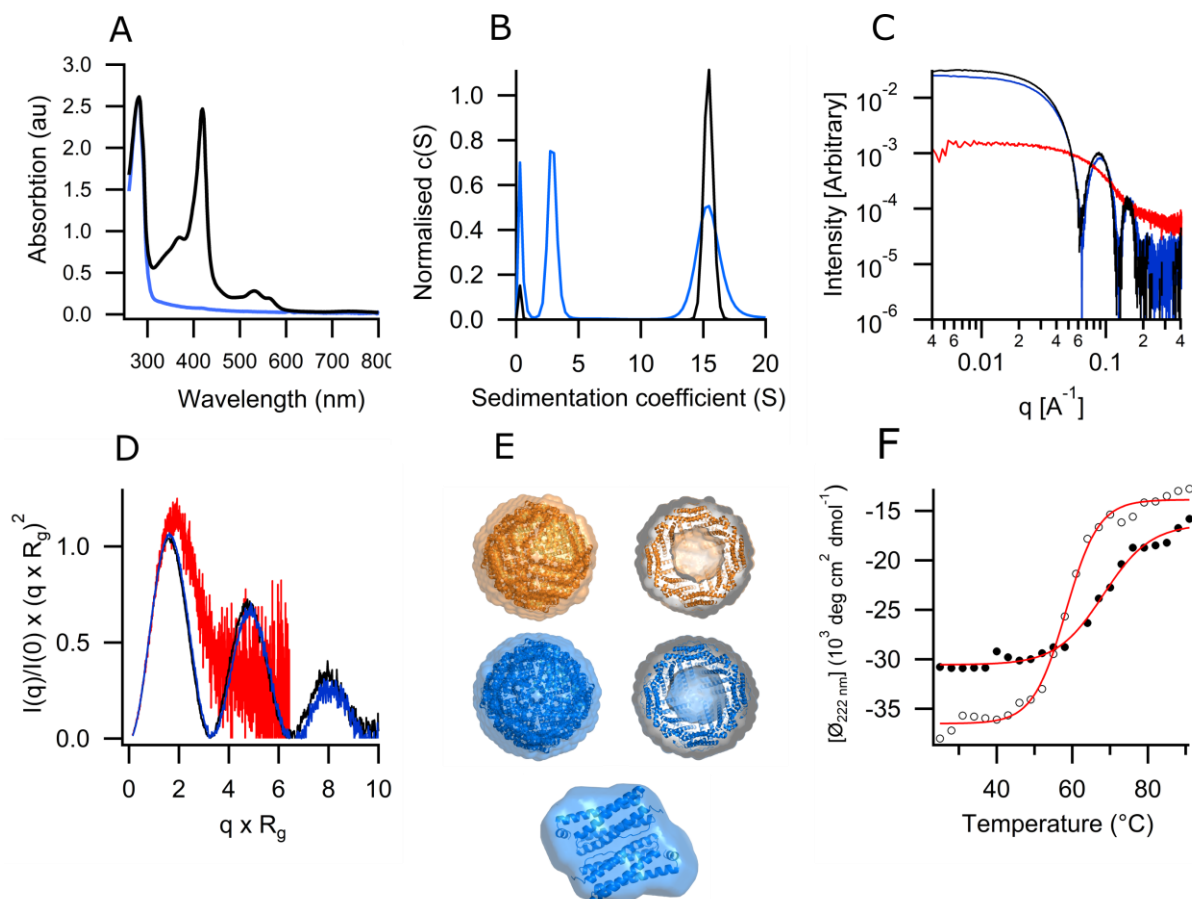


736
737 **Figure 4. Physicochemical characterization of ABfr and AABfr under ambient pressure. (A)**
738 UV/visible spectra of ABfr (black) and AABfr (blue). UV-visible spectra were recorded measured at a
739 protein concentration of approximately 50 µM in sodium phosphate buffer (45 mM NaPi, 250 mM NaCl,
740 pH 7). Curves are normalised to A280 = 1 to highlight differences in heme absorbance. **(B)** SV-AUC
741 c(s) distributions for ABfr (black) and AABR (blue). Sedimentation velocity was measured at a protein
742 concentration of approximately 50 µM in potassium phosphate buffer (45 mM KPi, 250 mM NaCl, pH
743 7) using a Beckmann ProteomeLab XL-I at 20˚C and 24000 rpm. Data was collected at a wavelength
744 of 280 nm. Data file time stamps were corrected using REDATE, and continuous sedimentation
745 coefficient (c(S)) distributions were fitted using SEDFIT. Buffer density ($\rho$ = 1.003 g cm$^{-3}$) and viscosity
746 ($\eta$ = 1.0107 mPa 865-) were measured using an Anton-Paar rolling ball viscometer. The protein partial
747 specific volume was calculated from the primary sequence ($\tilde{v}$ = 0.736 cm$^3$ g$^{-1}$). **(C)** HPLC-SAXS profiles
748 and **(D)** Kratky plots for ABfr icositetramer (black) and AABfr icositetramer (blue) and dimer (red). **(E)**
749 *Ab initio* bead model of ABfr (icositetramer, orange) and AABfr (icositetramer and dimer, blue), overlaid
750 with corresponding crystal structures (2VXI and 4CVP)[57,58]. Real space transformations were performed
751 using ScÅtter. The maximum diameter was determined by selecting values that resulted in high
752 reciprocal fit quality, and produced smooth, oscillation-free, real-space functions that decreased
753 smoothly to zero at high radius. A constant background was applied in the transformation, and real
754 space distributions were refined using the L1 norm of the Moore coefficients as a regularisation
755 target.The *ab initio* models were produced from refined pair distance distribution functions using
756 DAMMIF, and are DAMAVER averages of 23 runs. The models and crystal structures were visualized
757 using PyMOL. **(F)** Thermal denaturation far-UV circular dichroism spectra and fits for ABfr (open circles)
758 and AABfr (black circles). Data were collected at B23, Diamond Light Source, UK. Measurements were
759 performed in potassium phosphate buffer (45 mM, pH 7) at a protein concetnration of 0.5 g L$^{-1}$. Raw
760 data was converted to mean residue elipticity and secondary structure analysis was performed using
761 CAPITO.
762
763
764
765

766
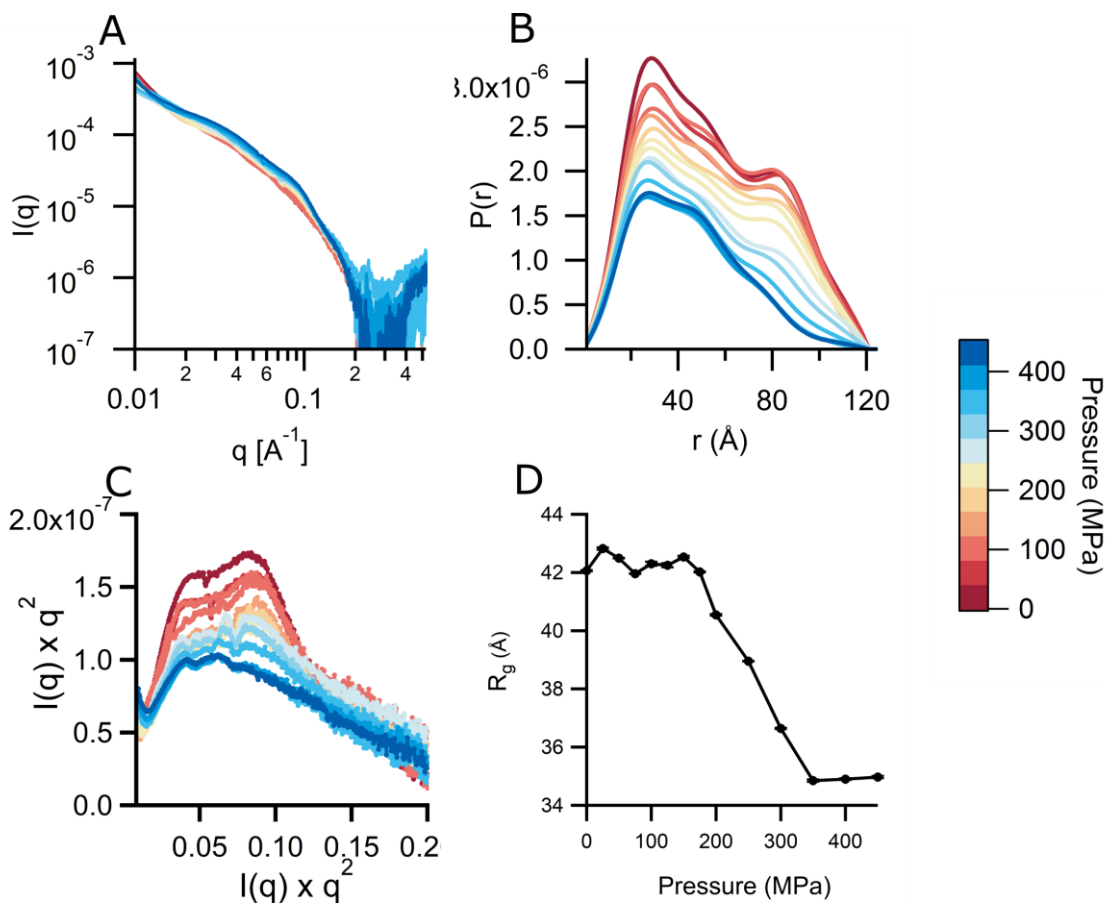
**Figure 5. Pressure dissociation of AABfr under equilibrium conditions between 0.1 and 450 MPa.**
**(A)** reciprocal space SAXS profiles, **(B)** Pair distance distribution (P(r)) functions, **(C)** Kratky plots and **(D)** Radius of gyration, $R_g$. SAXS data was collected between 0.1 MP (red) and 450 MPa (blue) at a protein concentration of 5 mg mL$^{-1}$ in 45 mM sodium phosphate buffer (pH 7). Real space transformations were performed using BAYESAPP, which uses Bayesian analysis to select parameters such as $D_{max}$ and data noise level.[74] $R_g$ was calculated from real space data.

773